Enhanced mechanical energy absorption via localized viscoplasticity of nano-cellular polymer coating under supersonic impact loading

Zongling Ren[1], Robert Green-Warren[3], Noah McAllister[3], Ara Kim[1], Asaad Shaikh[2], Assimina Pelegri[3], Jonathan P. Singer[3,§], Jae-Hwang Lee[1,2,*]

[1]Department of Mechanical and Industrial Engineering, University of Massachusetts, Amherst, MA 01003

[2]Interdisciplinary Graduate Program of Materials Science and Engineering, University of Massachusetts, Amherst, MA 01003

[3]Department of Mechanical and Aerospace Engineering, Rutgers University, Piscataway, NJ 08854

§ jonathan.singer@rutgers.edu

* leejh@umass.edu

Abstract:

Materials under viscoplastic deformation at ultrahigh strain rates (>10^6 s^{-1}) often demonstrate anomalous properties due to thermal and stress localization. As a model system, thermoplastic nano-cellular material (NCM) coatings are produced by consolidating microscopic polystyrene shells of nanoscale thin walls using self-limiting electrospray deposition. As both the spatial and temporal characterization scales are crucial, the NCMs are characterized by laser-induced projectile impact test (LIPIT) for understanding their ultrahigh-strain-rate plasticity originating from their porous structures. In LIPIT, supersonic collisions of rigid microspheres create these extreme physical conditions at the microscale. Viscoplastic vertical densification without the Poisson effect is the foremost process in the ultrahigh-rate plastic deformation of the NCM coatings. When the extreme nature of the viscoplastic deformation is promoted by increasing the porosity and reducing the thickness of NCM coatings, significantly more energy dissipation is observed without more material due to the localized feedback between adiabatic plastic deformation and thermal softening. Despite the stochastic and isotropic structural architecture of the NCM, the specific energy absorption of the NCM is high as 170 kJ/kg at the deformation speed of 400 m/s, which is attributed to the nanoscale effects from the thin wall thickness of NCM coatings. The findings suggest the general design rule for enhancing specific energy absorption by creating viscoplastic hot spots under impact loading.

1. Introduction

Cellular materials can enhance their mechanical performance via cellular geometries and surface states of the constituent medium.[1] Compared to their counterparts, homogeneous solid materials, whose properties are primarily determined by bulk properties, the physical properties of the cellular materials are tailorable through controlled inhomogeneity and anisotropy. Moreover, when cellular materials are generated with a certain uniformity, specific scaling trends exist in their physical properties, as witnessed by Ashby plots.[2] However, non-traditional scaling behavior can also exist if the characteristic length scale of the cellular structures, such as cell size, lattice constant, and wall thickness, is comparable to that of the constituent medium, like grain size or molecule size. In this aspect, the properties of the nano-cellular materials (NCMs) comprising nanoscale structural elements such as side walls or struts cannot be extrapolated by the ordinary scaling law based on the continuum mechanics, regardless of the cell sizes. For example, millimeter-scale cellular material made of nanometer-thick metallic tubes exhibits higher

specific strength with a new scaling exponent and an immense reversible compressive strain exceeding 50%.[3] Moreover, in the case of polymer NCMs, the mechanical properties can also be affected by the molecule size effect due to their macromolecular nature. Particularly, since the polymer chains near the surface can be more mobile,[4] the deformation behavior of polymeric NCMs can deviate from that of ordinary cellular materials. In addition to the spatial confinement and surface state of polymer chains, the large molecular weight of the polymer also creates strong strain-rate-dependent dynamics traditionally scaled by the time-temperature supposition.[5] However, high-strain-rate deformation of polymers accompanying large plastic strain is challenging to predict in this way because substantial adiabatic heating induced by the viscoplastic strain inevitably produces the coupling of the two dynamics. Moreover, the deformation can often be in the supersonic regime of cellular materials due to the substantially reduced sound speeds in cellular materials.[6] In this aspect, the high-strain-rate and large-strain deformation characteristics of polymer NCMs have not been explored much despite their potential applications in space, healthcare devices, aircraft, and energy storage.[7–9] Moreover, the NCM coating can inspire the development of protective materials for space protection applications as space debris density sharply increases due to accelerating human activities in Earth's orbits.[10–12] As minute space debris is not trackable due to its small size, people and spacecraft in space are inevitably exposed to damage caused by extreme collisions of such small debris.[13–15] For example, the micrometeoroid impact damage on one of the primary mirrors of the James Webb Space Telescope in May 2022 demonstrated the universal vulnerability to such threats.[16]

There has been ongoing interest in creating periodic NCMs having well-defined long-range ordered architecture via precisely controlled fabrication techniques to achieve high specific energy absorption.[17–19] For instance, periodic NCMs of epoxy with a diamond-like symmetry were fabricated by laser interference lithography, and their energy dissipation ability was quantified using nanoindentation.[19] Moreover, the periodic epoxy NCMs were also envisioned as energy-absorbing materials upon microscopic supersonic impact.[20] More recently, periodic carbon NCM was fabricated by pyrolysis of epoxy NCMs, and their energy absorption dynamics were investigated upon supersonic microprojectile impact.[21] Due to their regular geometries, the periodic NCMs were beneficial in understanding their distinct energy absorption mechanisms. However, the periodic NCMs can be challenging to deploy on a wide area with substantial surface roughness. In contrast, Kovacevich *et al.* demonstrated a class of polymer NCMs, that can be coated on nonplanar surfaces with a relatively uniform thickness via self-limiting electrospray deposition (SLED).[22,23] These polymer NCMs were aperiodic but exhibited good short-range ordering as they were produced by sequential deposition of hollow polymer shells having similar diameters. Moreover, as the wall thicknesses of the hollow shells are near 100 nm, they can serve as a model system for high-rate viscoplastic energy dissipation with the size effect.

2. Experimental Methods

2-1. Sample preparation by using self-limiting electrospray deposition (SLED)

Polystyrene (PS) (35 kDa and 280 kDa, Sigma-Aldrich) was used as received. 2-butanone (>99% Sigma-Aldrich) was used as received as the carrier solvent for the electrospray solution. Solutions were mixed to 1% wt. The SLED procedure generally follows the procedure by Green-Warren *et al.*[24] The SLED setup (see **Fig. 1a**) consists of a syringe pump (KD Scientific KDS-100), two high-voltage power supplies (Matsusada Precision Inc., RB30-30P), the stainless-steel delivery needle (SAI Infusion, 20 gauge, 1.5″), and the steel extractor ring (inner diameter of 20 mm and an outer diameter of 40 mm). The PS solution was delivered by a disposable syringe (5 mL NORM-JECT), connected to the spray delivery needle using polyethylene tubing. High-voltage potential supplies were connected to the delivery needle and the

extractor ring. The spray was collected on 2.5 cm × 2 cm rectangular silicon chips, which rested on 10 cm diameter silicon wafers (both University Wafer, Boron-doped P-type 0-100 Ohm-cm). The base wafer was electrically grounded during the spray. The silicon chips were diamond scribed on the back of the chip to facilitate post-spray fracturing. The scribing line was parallel to the long edge of the chip and located in the middle of the chip. All silicon wafers and chips were cleaned and degreased with ethanol and acetone prior to SLED. Taylor-cone jet sprays were used for all samples. The driving voltage on the delivery needle was set to 6.0 kV. The extractor ring voltage was varied between 3.8 – 4.0 kV in order to maintain the stability of the Taylor cone. The needle tip-to-sample spray distance was set to 4 cm, and the extractor ring was located 1 cm above the needle tip. A flow rate of 0.5 mL/h was used for all samples. The substrate temperature was set to target temperatures using a hotplate. The relative humidity was monitored and ranged between 29.2 to 33.7%. A full table of experimental parameters can be found in **Table S1**. **Fig. 1b** shows a scanning electron microscope (SEM) image of a typical NCM sample after focused ion beam (FIB) milling.

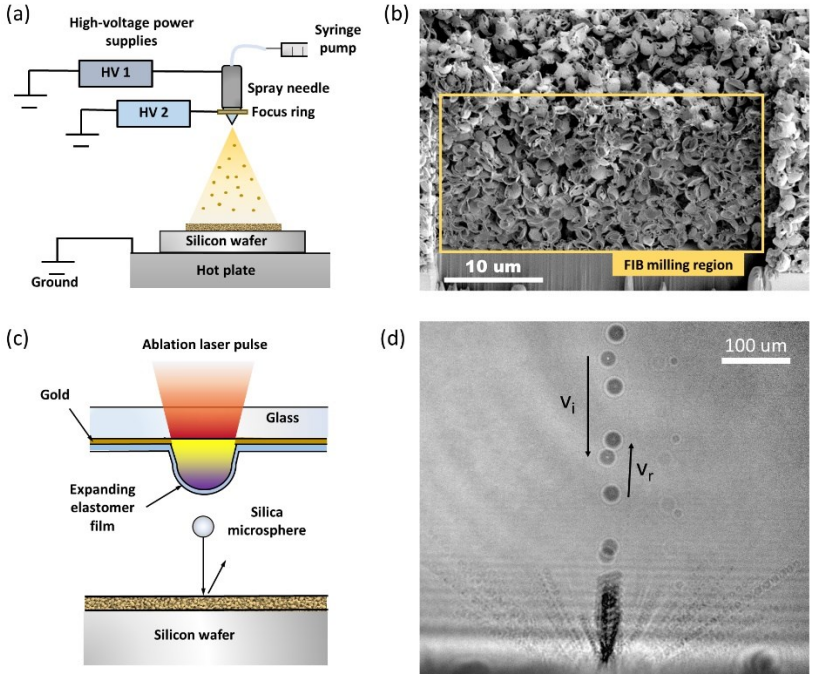

Figure 1 (a) Schematic diagram of SLED. (b) Cross-sectional SEM image of PS-NCM. (c) Schematic diagram of LIPIT (d) An ultrafast stroboscopic micrograph shows collision motions of a 540 m/s projectile and ejecta from a specimen.

2.2 Ultra-high-strain rate impact testing

A microballistic method called laser-induced projectile impact test (LIPIT)[24–26] has widely been used to apply a localized high-strain rate and high-strain deformation on microscale specimens. The LIPIT (see **Fig. 1c**) was used for microscopic ballistic experiments in which a PS NCM sample was impacted by a single silica microsphere (radius, R_p= 9.8 μm) accelerated to have an impact velocity (v_i) ranging from 100 to 800 m/s by laser ablation of a launching pad. Besides the projectile and target sample, the LIPIT experiment needs a launchpad containing gold and cross-linked polydimethylsiloxane (PDMS) protecting film. In LIPIT characterization, the laser ablated the gold to vaporize, then propelled the micro-projectile (silica microsphere) to impact the target specimen. The gold film on our launchpad was approximately 60

nm thick and deposited with a sputter coater (Desk V, Denton Vacuum). The PDMS film was spin-coated prior to cross-linking. The collision process was observed during the impact with ultrafast stroboscopic imaging. A typical stroboscopic micrograph in **Fig. 1d** by 20 illumination pulses shows single particle dynamics through the entire collision process. As the field of view of the image was calibrated, v_{i} and v_{r} could be calculated using the distance between the nearest particle positions (Δz) and the time duration (Δt) between two adjacent illumination pulses. Δt was selected within a range of 263 – 892 ns.

2.3 Nanoindentation testing for quasi-static deformation

Nanoindentation was utilized to observe the quasi-static deformation properties of NCMs and to compare them with microballistic deformation characteristics under ultrahigh strain rates. A conospherical indenter tip, with a nominal radius of 10 μm and 60° inclusion angle, was implemented for the quasi-static loading of the NCM films. These experiments were conducted in an electromagnetic indentation system (MicroMaterials NanoTest Vantage). For the indention of NCM samples, two samples of ~80% porosity sprayed at room temperature (~20 °C) were measured. The NCM samples were approximately 16 μm and 22 μm thick. This difference in thickness can be attributed mainly to the thickness variation inherent in the SLED process and the scattering effects of the microstructure when measuring the thickness via optical microscopy. Indentation experiment schedules were set to a trapezoidal load sequence of 30s-30s-30s, with a peak load of 10 mN and varying loading/unloading rates such that the load/unload times were held constant for each indent. The loading sequence described represents constant loading and unloading times of 30 seconds and a hold time at a peak load of 30 seconds. This was done to mitigate transient deformation artifacts, commonly observed at the onset of unloading for short hold times of viscoelastic materials evaluated via nanoindentation. For each sample, a 5×10 and 10×10 indentation grid pattern was employed with 300 μm spacing between each indent. Energy dissipation was selected as the comparative parameter for ascertaining the effects of strain rate on the mechanical properties of NCM films. The work of indentation, characterized as the area under the load/unload curves, was calculated and taken as energy dissipation. The specific energy dissipation of nanoindentation was computed for each indent by normalizing the estimated energy dissipation by the indentation contact area as projected from SEM images. This was done by assuming that the visibly deformed zone constituted the diameter of a cylinder of deformed mass.

3. Results and Discussion

3.1 Structural characteristics depending on SLED conditions

Two groups of samples were prepared with (1) varying spray times (connected with areal mass) and (2) spray temperatures (connected with areal mass and absolute density). While spraying, other SLED conditions, including solution concentration (1 wt%), flow rate (0.5 mL/s), and applied voltages, were the same. For the spray-time-dependent SLED, all samples were produced with the same spray temperature (~20 ºC room temperature) but with different spray times. The sample's thickness (h) was measured by fracturing its spray center at room temperature. The sample was then mounted vertically on a square steel reference block using vacuum grease (Dow Corning) as a surface adhesive, such that the spray was on the outside of the block and the cross-sectional surface faced upward. The sample was then imaged in an optical microscope (Leica DM2700 M with a Leica MC170 HD camera) in three locations spaced ~8 mm apart along its length. Optical images were taken in both reflection and transmission modes; the image's focal plane remains constant. Porosity ϕ was calculated using $\phi = 1 - \frac{h_{\mathrm{dense}}}{h_{\mathrm{porous}}}$, where h_{dense} and h_{porous} are

the thickness measured using an optical reflectometer (Filmetrics F40-EX) and the thickness measured using the optical microscope technique, respectively. [23,27] As the name of this method suggests, the SLED produces samples with a self-limiting thickness. This self-limiting occurs due to the gradual deposition of charge in the forming film, which depends to some extent on environmental parameters, such as the removal of spray solvent by the hood air flow and specific placement of the silicon chip. Consequently, the sample thickness and porosity will vary to some extent, even for the same spray time. Therefore, each sample sprayed with different parameters must have the porosity and thickness measured individually. The observed trend of h and ϕ, along with the change of the spray time, is shown in **Fig. 2a**. As the spray time increased, h monotonically increased, with a porosity of 76.1±4.1%. Thus, the samples produced by the spray-time-dependent method were used for the thickness series of NCM samples with a presumed fixed mean porosity of 76.1 %. For the spray-temperature-dependent SLED, three samples were prepared at three different spraying temperatures, room temperature, 75, and 95 °C, with a fixed spray time of two hours. In contrast to the spray-time-dependent SLED, the spray temperature affected both h and ϕ (**Fig. 2b**) due to the effect of sample mobility on charge dissipation and final morphology in SLED.[28] As in **Fig. 2b**, the porosities varied from almost 70 % to zero.

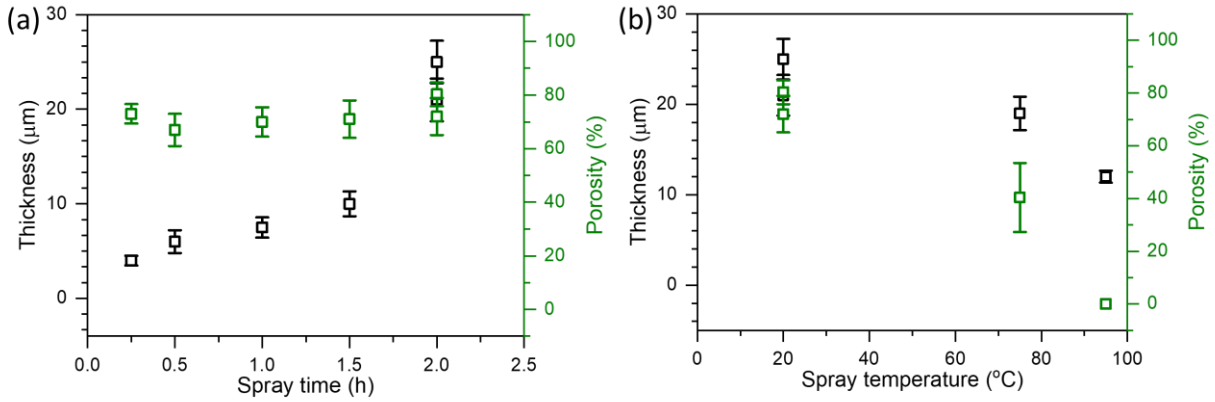

Figure 2 The thickness and the porosity variation depend on (a) spray time and (b) spray temperature. The porosities for 20 °C and 75 °C are 76 % and 40%, respectively, while 95°C spray results in a nonporous coating.

The five samples in **Table 1** were fabricated using the SLED control parameters. Their areal density (ρ_A) were calculated using the density of PS (ρ=1,050 kg/m^3) and h. PS-0012 and NCM-4018 were used for ϕ-dependent mechanical properties as their areal density (ρ_A) were very similar. NCM-8021, -7108, and -6806 were used for h-dependent mechanical properties as their ϕ were varied insignificantly.

Table 1 Structural parameters of the tested NCM samples. The primary control parameters are shown in bold. The naming convention indicates these parameters as sample type-(sample porosity)(sample thickness).

Sample	ϕ (%)	h (μm)	ρ_A (g/m^2)	ID #
PS-0012	**0**	12	12.6	#27
NCM-4018	**40**	19	12.0	#26
NCM-8021	80	**21**	4.4	#74

NCM-7108	71	**8**	2.4	#76
NCM-6806	68	**6**	2.0	#77

3.2 Kinetic characteristics

Spectra of v_r were measured up to 800 m/s by LIPIT for different ϕ values of samples, 0 and 40 % (**Fig. 3a** and **3b**). The two PS samples had approximately the same areal density of 12.3 g/m^2. A bare silicon substrate without any PS samples was also tested for reference. The v_r-spectrum of the silicon substrate was the most elastic, and the two PS samples exhibited less elasticity than the silicon substrate regardless of ϕ. v_r of the nonporous PS layer (PS-0012) gradually decreased until v_i reached 500 m/s and rapidly started to increase from 500 m/s. This non-monotonic trend originated from the dominant plastic contribution of the PS layer at the low-v_i regime, and the elastic contribution of the Si substrate at the high-v_i regime. Interestingly, a similar trend was observed in the supersonic collision of PS microspheres with PS substrate.[29] As ϕ was increased to 40 % in NCM-4018, v_r was reduced to close to zero in the low-v_i regime less than 300 m/s. The inelastic character revealed in the v_r spectrum can be visible more distinctly in the spectrum of coefficient of restitution (CoR), v_r/v_i, in **Fig. 3c** and **3d**. The CoR spectrum of the Si substrate showed a monotonically decreasing trend down to 0.5 within the tested range of v_i. This growing inelasticity implies that the silica microsphere and Si substrate underwent internal fractures during the energetic collision. The CoR spectrum of PS-0012 exhibited a more severe inelastic trend in the v_i range up to 500 m/s due to plastic deformation of PS. As the silica microsphere made a more profound impression close to the surface of the Si substrate, the growing elastic contribution from the Si substrate overturned the CoR trend at 500 m/s. Compared to PS-0012, the CoR spectrum of NCM-4018 had extremely low elasticity at the low v_i range (< 200 m/s). As v_i increased, NCM-4018 was more compacted, and the impactor more profoundly interacted with the Si substrate, resulting in the CoR values close to those of the silicon substrate.

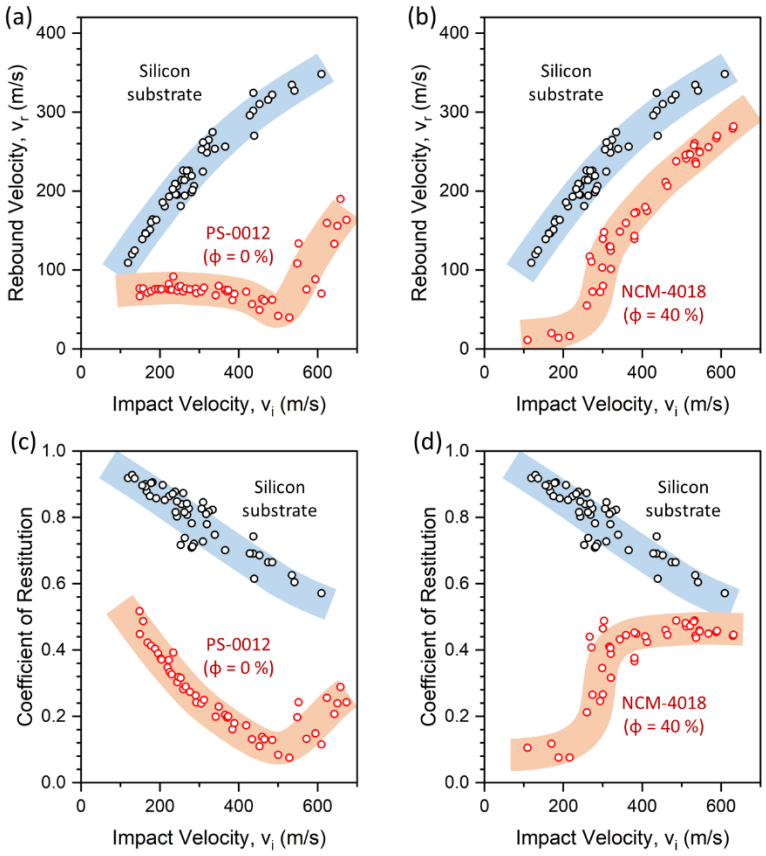

Figure 3 Collision characteristics of PS NCM samples depending on ϕ. The v_r spectra of PS NCM coating having ϕ of (a) 0 % and (b) 40 % are plotted with that of a bare silicon substrate as a reference. (c) – (d) CoR spectra corresponding to the v_r spectra are plotted.

The v_r-spectra of the NCMs, primarily depending on their thicknesses, are shown in **Fig. 4a**. Since their ϕ values were similar, the three NCM samples showed a similar overall trend for v_r to systematically decrease as ϕ increased. In the CoR-spectra (**Fig. 4b**), a thinner NCM approached the CoR trend of the Si substrate at a lower v_i. Interestingly, the thickest sample, NCM-8021, showed zero CoR as the silica microspheres were captured at the low v_i range. The particle capture was not observed from the 6 μm thick NCM-6806 and was more consistently observed from the 21 μm thick NCM-8021. When ϕ was fixed, the thicker thickness directly increased NCM's areal density, which led to the enhanced capacity of impact energy dissipation of NCM. Moreover, as the thickness of NCM exceeded the radius of the impactor (~10 μm), an additional shear contact at the silica microsphere's sides might promote the microsphere capture.

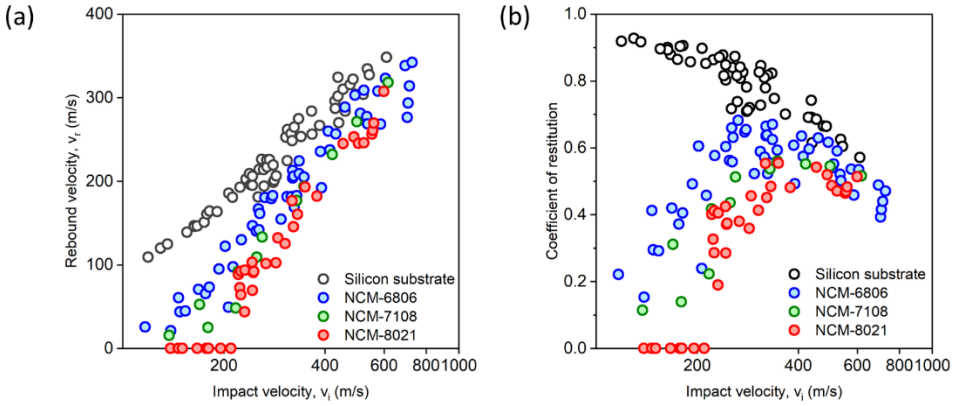

Figure 4 The collision characteristics of NCMs depend on thickness. The trends of (a) impact velocity vs. rebound velocity and (b) Coefficient of restitution. The trend variation among samples with different thicknesses is insignificant.

3.3 Characteristic impact energy absorption

The collisions of the silica microsphere on a bare Si substrate produced considerable energy dissipation according to their v_r and CoR spectra. When a PS specimen is present, the Si substrate dissipates a different amount of energy under the same v_i event. Thus, the total energy dissipation may include the contribution of an unknown nonlinear coupling of the PS specimen and Si substrate. Therefore, the actual amount of energy dissipation by the PS sample cannot be calculated by linear subtraction of the energy dissipation of the bare Si substrate at the same v_i. Despite this limitation, the spectrum of energy dissipation ($\Delta E = E_i - E_r$) in a collision from the bare Si substrate is still helpful as a baseline for the enhancement effect in energy dissipation by the presence of the NCM layer. The ΔE-spectrum of the Si substrate is shown in **Fig. 5a** with its fitting curve,

$$W_{Si}(v_i) = a_1 E_i \left[1 - a_2 \exp\left\{-\left(\frac{v_i}{a_3}\right)^2\right\}\right], \quad (1)$$

where the three fitting parameters, a_1, a_2, and a_3, are 0.76 ±0.05, 0.82 ±0.06, and 425 ±51, respectively. Due to the energy conservation, ΔE must be equal to or less than the impact kinetic energy (E_i). **Eq. 1** was phenomenologically introduced to show the nonlinear trend of the ΔE-spectrum from the bare Si substrate. The observed energy dissipation trend was mainly attributed to the plastic deformation caused by the crazing (fine cracks),[30] primarily within the glassy silica microsphere. While **Eq. 1** provides the characteristic trend of the collision without NCM, it can be neither zero (total elastic) nor E_i (total inelastic) for the two asymptotic limits of v_i, 0 and ∞. It implies that **Eq. 1** can be used in this study where v_i was sufficiently higher than a transition velocity associated with the elastic limit of a silica microsphere and was lower than another transition velocity associated with penetration or catastrophic fragmentation failure of the silica microsphere. The enhanced energy dissipation, $\Delta E(v_i) - W_{Si}(v_i)$, was normalized by ρ_A and a cross-sectional area of the projectile (πR_p^2) for specific energy dissipation, ΔE^*:

$$\Delta E^* \equiv \frac{\Delta E - W_{Si}}{\rho_A (\pi R_p^2)} \quad (2)$$

Note that the use of ρ_A for the normalization factor implies that the entire material under the projectile is contributed to ΔE regardless of h. This approximation becomes more realistic as a sample gets thinner or v_i becomes higher. In our study, all the NCMs were relatively thin ($h \leq 2R_p$) and most v_i were fast (transonic or supersonic). Additionally, compared to the case of bare Si substrate, the Si substrate

contributed less when an NCM sample was present. Thus, for the current study, where the quantification of the true material volume contributing to ΔE was challenging, **Eq. 2** was employed as a conservative quantification method of ΔE^*. The specific energy dissipation (ΔE^*) is essentially the same definition as the specific penetration energy widely used in LIPIT penetration experiments.[31–33] Thus, ΔE^* can serve as a figure of merit for the effectiveness of the NCM's mass in enhancing ΔE. The ΔE^*-spectrum of PS0012 in **Fig. 5b** was very monotonic without much fluctuation up to 500 m/s due to its nonporous nature. NCM-4018 produced an insignificant enhancement in ΔE^* at a low v_i range and became noticeably ineffective above 300 m/s, compared to the nonporous PS. As ϕ increased from 40 to 80% in NCM-8021, a substantial enhancement was observed but still underperformed than the nonporous PS above 400 m/s. We suppose this enhancement was mainly driven by an increase (~100%) of ϕ rather than an increase (~17%) of h. Moreover, as this implies that the NCM of higher ϕ induced more viscoplastic deformation per volume, we suppose that very intense viscoplastic zones or hot spots had been produced in the deformation of the high porosity NCM. More enhancement (as high as twice) was observed in NCM-7108 by a 160 % reduction of h. The ΔE^*-spectrum of NCM-7108 surpassed that of PS-0012 as high as eight times within the entire range of tested v_i. The reduced deformed volume of NCM, commensurate with h, resulted in more viscoplastic deformation per volume and, in other words, more extreme hot spots. When h was further reduced from 8 to 6 μm in NCM-6806, the additional enhancement was not apparent, and its trend became very fluctuating for v_i > 200m/s. The ΔE^* results were compared with the published LIPIT results of nanoarchitected carbon created by two-photon lithography followed by vacuum carbonzation.[26] While ΔE^* of NCM7108 reached 170 kJ/kg at 400 m/s, the nanoarchitected carbon (regarded as periodic NCMs) demonstrated near 400 kJ/kg under the same v_i. According to the uniaxial compression testing of epoxy nanoframes and their carbonized nanostructures (regarded as periodic epoxy and carbon NCMs), $\Delta E^*$was enhanced more than 50% after carbonization under the quasi-static loading condition.[21] Thus, the demonstrated ΔE^* of NCM7108 can be promising as it was realized by stochastic polymeric NCMs fabricated by ambient, bottom-up processing of commodity thermoplastic. One can consider the ejecta or debris from NCM, as shown in **Fig. 1(d)**, may carry a substantial portion of the initial kinetic energy. Although the debris were visually overwhelming, their velocities were below 10% of the primary projectile's kinetic energy in **Fig. 1(d)**. It implies that the kinetic energy sum for all debris cannot exceed 1% of the initial kinetic energy, even if the sum of all ejecta masses were the same as that of the primary projectile. Thus, the ejecta's kinetic energy was not considered one of the major energy dissipation processes. For comparison, a specimen similar to NCM8021 was characterized by nanoindentation. Through the severe indentation approaching to the bottom of the specimen, ΔE^* was measured to be 14.3±0.4 kJ/kg, where the loading and unloading curves and the resultant indentation volume were used (see **Fig. S1** and **S2** for details). ΔE^* from the quasi-static compression was similar to the lowest ΔE^* value of the LIPIT data. Since the achievable range of ΔE^* is limited to E_i, the energy dissipation efficacy, η, is defined by

$$\eta \equiv \left(\frac{\Delta E - W_{\mathrm{Si}}}{E_\mathrm{i}}\right)\frac{1}{\rho_\mathrm{A}} \tag{3}$$

η indicates a dissipated fraction of the impact energy by the unit areal density of a protective coating (*i.e.*, an NCM layer). Since E_i can implicitly compensate the projectile size effect in energy dissipation, the explicit correction factor such as πR_p^2 in Eq. (2) is not used for η. The η-spectra in **Fig. 5c** of all the PS samples were monotonically decreasing as v_i increased regardless of their structural parameters. The trends of η were well represented by the sigmoid function,

$$\eta \cong \frac{\eta_0}{1+(v_\mathrm{i}/v_\mathrm{c})^3} \tag{4}$$

In the fitted curves, η_0 is the asymptotic value for $v_i \cong 0$, and v_c is the critical velocity beyond which η reduces rapidly with a slope of v_i^{-3}. NCM-6806 was not included in this fitting due to its unstable fluctuation. In **Fig. 5d**, the changes in the two fitting parameters, η_0 and v_c between PS-0012 and NCM-8021 were dominantly driven by ϕ, while the changes between NCM8021 and NCM-7108 were mainly driven by the reduction of h. Substantial reduction in v_c but with a limited enhancement of η_0 was observed from the intermediate porosity (ϕ=40%). It implies that the deformation behavior was close to nonporous PS, and the introduced pores could not enhance sufficient plastic deformation. However, the high porosity NCM (NCM-8021) made a noticeable up-shift in η_0 with a subtle reduction in v_c. Further promotion of η_0 without much reduction of v_c was possible by reducing h in NCM-7108.

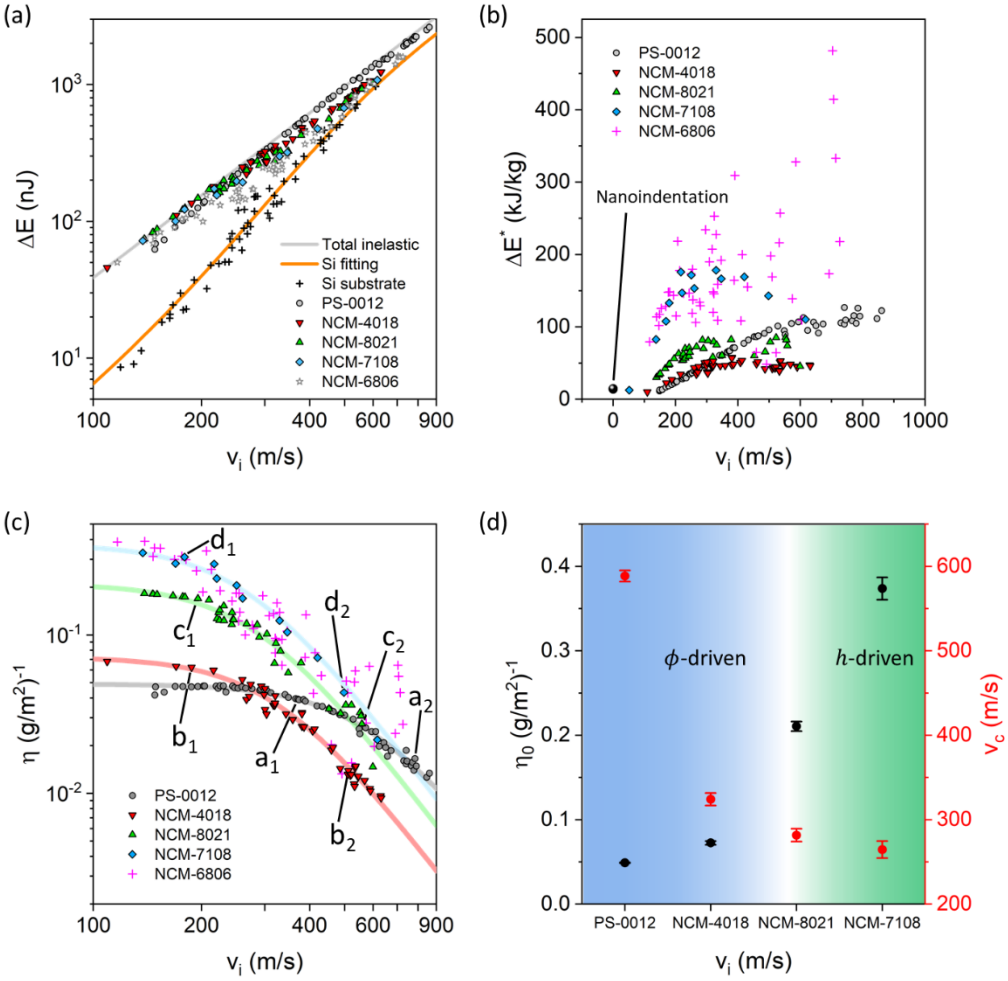

Figure 5 Collision dynamic characteristics of NCM samples depending on ϕ and h. (a) The ΔE-spectra of all tested specimens are plotted with that of the Si substrate. The fitting curve for the Si substrate from Eq. (1) provides a baseline of ΔE. The total inelastic line indicates the upper limit of ΔE. (b) The ΔE^*-spectra compare the energy dissipation capability enhanced from the bare substrate. (c) The η-spectra are plotted with their fitting curves based on Eq. (4) except NCM-6806. The labels correspond to the SEM images in Fig. 6. (d) The trends of η_0 and v_c from the fitting curves are plotted with their errors. The color gradient from blue to white and white to green indicates whether the changes are made by ϕ or h.

3.4 Impact-induced structural responses

Post-impact structural features of the collision site provide essential knowledge in energy dissipative responses of PS NCMs. Representative SEM images of the tested samples below and above v_c are shown in **Fig. 6**. All the NCM samples were densified without noticeable damage features beyond the direct contact region when $v_i < v_c$. As v_i substantially exceeded v_c, exposed Si substrates were commonly observed at the bottom of the craters. This observation confirms that the trend of v_i^{-3} in the η-spectra in **Fig. 5c** originated from the mechanical interaction with the Si substrate. Extensive pile-ups and radial cracks were found at the crater of PS0012 due to the displaced material by a silica microsphere impression. The pile-ups and cracks were negligible in NCM4018 as the microsphere impression volume could be accommodated via densification. More extensive or non-localized damage features were observed in the areas beyond the direct impact regions of the highly porous samples (NCM8021 and NCM 6806). The material losses in the NCMs were caused mainly by the adhesion of molten PS to the rebounding silica microsphere and debris ejection. Occasionally, impact-induced elastic waves propagating in the Si substrate also caused circular delamination or spallation of specimens[34] (see **Fig. S3**). Various mechanical waves generated by the projectile's collision could be essential in materials' deformation and damage processes, mainly when interferences existed with their reflected waves from mechanical interfaces. For the NCMs in this study, their estimated acoustic wave speeds were significantly slower than the nonporous one. For example, NCM8021 was supposed to have a longitudinal elastic wave (foremost wave) speed of 360–450 m/s, according to $\sqrt{E/(1-\phi)\rho}$, where E (28–42 MPa) was the elastic modulus of the NCM (ϕ~80%). [24] As the impact-induced deformation of NCMs had to be localized near the advancing microsphere, the multiple-wave interference effect was not importantly considered.

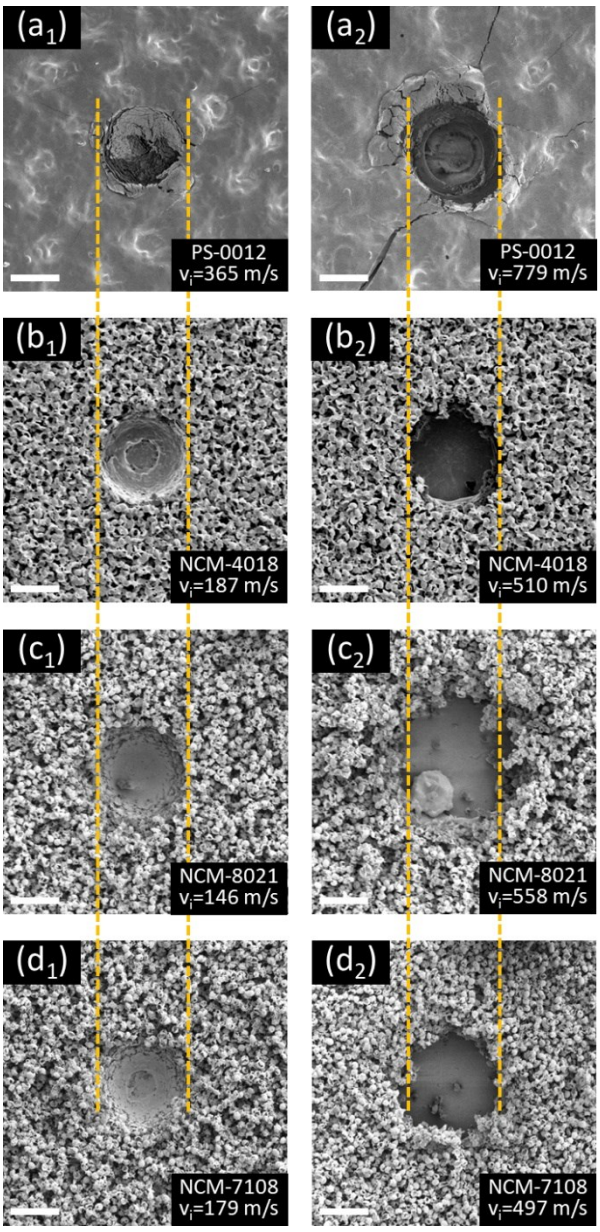

Figure 6 The SEM images of impact craters of PS-0012 (a_1 and a_2), NCM-4018 (b_1 and b_2), NCM-8021 (c_1 and c_2), and NCM-7108 (d_1 and d_2). The first column of the images displays impact craters with lower impact velocities ($v_i < v_c$), and the second column shows those with higher impact velocities ($v_i > v_c$). The yellow dashed lines indicate the diameter of the silica microspheres. All the scale bars are 10 μm.

The NCMs comprised 100 – 200 nm thick PS spherical shells (see **Fig. S4**). The shells collapsed, were densified, and partially melted (**Fig. 7a**) during the adiabatic plastic deformation by the spherical projectile in LIPIT. **Fig. 7b** shows the transition region from a complete to a partial melting zone. The nanoscale cracks and melting regions between cracks indicate the existence of hot spots during the compressive shear deformation, as we supposed in the earlier discussion. This densification-driven plastic deformation of NCM must be highly energy-dissipative compared to the continuous plastic deformation in nonporous PS-0012 to explain the significantly high η_0 values of the NCMs. Note that Boyce *et al.* reported a significantly enhanced hysteresis in stress-strain loops of thermoplastic polyurethanes as the strain rate

increased.[35] Since the thermoplastic polyurethane was a heterogeneous polymer of glassy and rubbery phases, the coexistence of glassy and rubbery phases could be attributed to the larger hysteresis (or more energy dissipation). Although the NCMs in this study were made of PS homopolymer, the localized hot spots could produce a heterogeneous state of glassy and rubbery that could enhance energy dissipation. More recently, in the temperature-controlled LIPIT, Veysset *et al.* reported that the impact-induced glass-to-rubbery transition of polyurea occurred and created higher energy dissipation upon impact.[36] Thus, the heterogeneous material state of NCMs through the localized glass-to-rubbery transition at the hot spots can enable more energy dissipation. For comparison, an NCM specimen (h ~23 μm) was quasi-statically indented with a 10 μm radius spheroconical indenter. Due to the high level of surface contact between plastically deformed shells and the indenter, there was evidence suggesting that regions of the film detached from the sample film and were later redeposited in a future indentation (**Fig. S5**). When examining the material that appears to have been redeposited (**Fig. 7c**), which reflects the behavior of the sample immediately beneath the indenter, there was no evidence of melting at the feature's center (**Fig. 7d**), which was very common in the impact-induced craters in **Fig. 6**. The indentation center also showed a very smooth surface following the spherical contact geometry, which implies the propagation of plastic flows was faster than the indentation speed. In other words, the rough surface of insufficient compaction in **Fig. 7a** indicates that impact-induced plastic flows did not propagate fast enough compared to the speed of a silica microsphere. The differences in the deformation features imply that the compressive deformation in an NCM proceeded with negligible lateral displacement of shells (or localization of plasticity) in LIPIT. As the ultrahigh rate deformation of NCMs occurred under this temporal confinement effect, the shells could be densified with more severe adiabatic shear deformation with viscoplastic hot spots. Consequently, PS shells

This extreme nature of deformation was essential for the observed high η values.

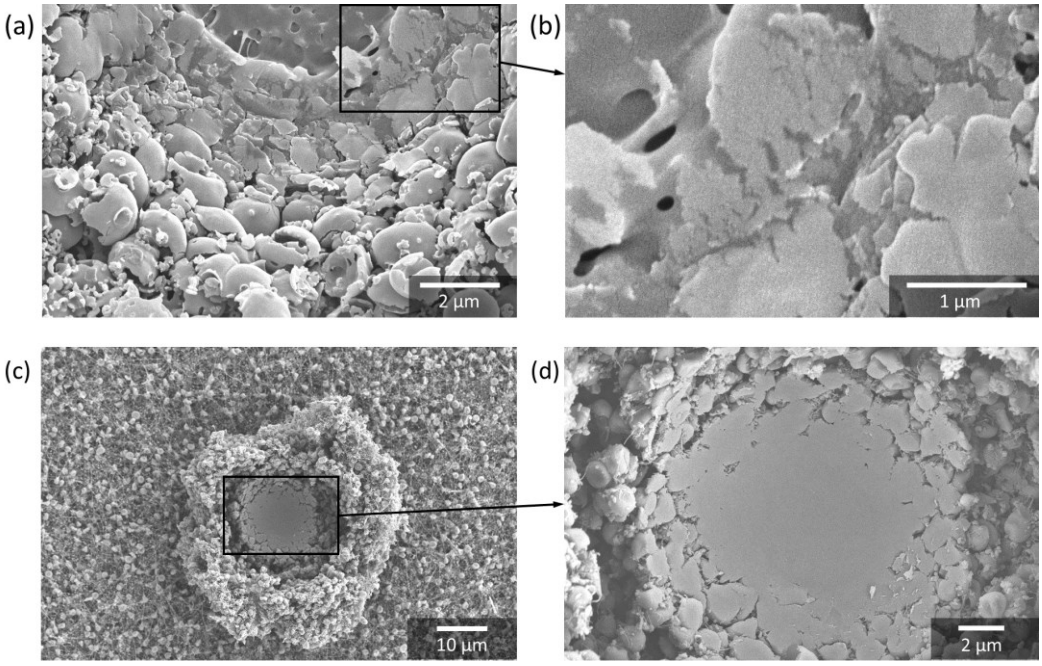

Figure 7 Comparison of deformation features created by LIPIT and nanoindentation. (a) Bottom half-view SEM image of a crater of NCM-6806 produced after a 146 m/s impact and (b) a magnified view of the

boxed region in (a). (c) Low magnification SEM image of a crater produced by a conospherical indenter (diameter 20μm). (d) Magnified view of the crater in (c).

4. Conclusion

The ultrahigh-rate mechanical study was performed using the microballistic method for PS NCM films produced by SLED, a scalable and conformal coating technique. The ultrahigh rate deformation of the NCM films dominantly produced viscoplastic vertical densification without a noticeable Poisson effect. Due to the adiabatic shear process, the PS NCM films consistently underwent melting at the impact center. True enhancement in impact energy absorption was possible by two design approaches, increasing porosity and reducing coating thickness, as more extreme viscoplastic deformation was created. The reduced coating thickness led to premature saturation of energy absorption capability; however, it was compensated by improved energy dissipation efficiency. Furthermore, the nonlinearly increasing trend of energy dissipation efficiency with increasing porosity may indicate nanoscale effects originating from the wall thickness of the shell. Considering the scalable coating possibility of the PS NCMs, the specific energy absorption of NCMs reaching 170 kJ/kg at 400 m/s is notable compared to previously reported values of periodic carbon lattices fabricated by laser-based lithography. We believe that various modifications on NCMs, such as cross-linking, carbonization, oxidation, and passivation, can enhance specific energy absorption further. As mentioned above, it is critical to emphasize that this energy density was possible without complex optical patterning, designer photochemistry, high temperature, or controlled-environment post-processing. Instead, the demonstrated processing was ambient and used commodity polymer in a universal solvent, which could be reclaimed via condensation in a more advanced manufacturing scenario. Indeed, this approach could be employed to upcycle waste PS foam from packing materials into protective coatings. Further, to our understanding, there is nothing particular about PS to the observed mechanisms, and it is expected that bioderived thermoplastics, such as polysaccharides or proteins, can serve as green NCM coatings through this process.

Declaration of competing interest

The authors declare that they have no known competing financial interests or personal relationships that could have appeared to influence the work reported in this paper.

Acknowledgements

Finantial support by the National Science Foundation (CMMI-2019928 and CMMI-2019849) is gatefully acknowledged.

Supplimentary materials

Supplementary material associated with this article can be found, in the online version.

References

1. Sampath, U. G. T. M., Ching, Y. C., Chuah, C. H., Sabariah, J. J. & Lin, P. C. Fabrication of porous materials from natural/synthetic biopolymers and their composites. *Materials* **9**, 1–32 (2016).

2. Wegst, U. G. K., Bai, H., Saiz, E., Tomsia, A. P. & Ritchie, R. O. Bioinspired structural materials. *Nat Mater* **14**, 23–36 (2015).
3. Schaedler, T. A. *et al.* Ultralight metallic microlattices. *Science (1979)* **334**, 962–965 (2011).
4. Hyon, J. *et al.* Extreme Energy Absorption in Glassy Polymer Thin Films by Supersonic Micro-projectile Impact. *Materials Today* **21**, 817–824 (2018).
5. D.Ferry, J. *Viscoelastic Properties of Polymers*. (1980).
6. Kovalenko, M. V., Protesescu, L. & Bodnarchuk, M. I. Properties and potential optoelectronic applications of lead halide perovskite nanocrystals. *Science (1979)* **358**, 745–750 (2017).
7. Cheng, H. *et al.* Multifaceted applications of cellulosic porous materials in environment, energy, and health. *Prog Polym Sci* **106**, 101253 (2020).
8. Duzellier, S. *et al.* Space debris generation in GEO: Space materials testing and evaluation. *Acta Astronaut* **192**, 258–275 (2022).
9. Slater, A. G. & Cooper, A. I. Function-led design of new porous materials. *Science (1979)* **348**, aaa8075 (2015).
10. Esmiller, B., Jacquelard, C., Eckel, H.-A. & Wnuk, E. Space debris removal by ground-based lasers: main conclusions of the European project CLEANSPACE. *Appl Opt* **53**, l45 (2014).
11. Gorman, A. Robot avatars: the material culture of human activity in Earth orbit. in *Archaeology and heritage of the human movement into space* 29–47 (Springer, 2015).
12. Krisko, P. H. The predicted growth of the low-Earth orbit space debris environment - An assessment of future risk for spacecraft. *Proc Inst Mech Eng G J Aerosp Eng* **221**, 975–985 (2007).
13. Božić, O., Eggers, T. & Wiggen, S. Aerothermal and flight mechanic considerations by development of small launchers for low orbit payloads started from lorentz rail accelerator. *Progress in Propulsion Physics* **2**, 765–784 (2011).
14. Smith, C. T. G. *et al.* Complete Atomic Oxygen and UV Protection for Polymer and Composite Materials in a Low Earth Orbit. *ACS Appl Mater Interfaces* **13**, 6670–6677 (2021).
15. Sotskiy, M. Y., Veldanov, V. A. & Selivanov, V. V. Growth in the quantity of debris in Space as AN effect of mutual mechanical collisions of various types. *Acta Astronaut* **135**, 10–14 (2017).
16. Cesari, T. Webb: Engineered to Endure Micrometeoroid Impacts. *NASA Goddard* https://blogs.nasa.gov/webb/2022/06/08/webb-engineered-to-endure-micrometeoroid-impacts/ (2022).
17. Ha, N. S. & Lu, G. A review of recent research on bio-inspired structures and materials for energy absorption applications. *Compos B Eng* **181**, 107496 (2020).
18. Si, Y., Yu, J., Tang, X., Ge, J. & Ding, B. Ultralight nanofibre-assembled cellular aerogels with superelasticity and multifunctionality. *Nat Commun* **5**, (2014).
19. Singh, G., Sarin, R. K. & Raj, B. A novel robust exclusive-OR function implementation in QCA nanotechnology with energy dissipation analysis. *J Comput Electron* **15**, 455–465 (2016).

20. Lee, J. H., Wang, L., Kooi, S., Boyce, M. C. & Thomas, E. L. Enhanced energy dissipation in periodic epoxy nanoframes. *Nano Lett* **10**, 2592–2597 (2010).
21. Lee, J. H., Singer, J. P. & Thomas, E. L. Micro-/nanostructured mechanical metamaterials. *Advanced Materials* **24**, 4782–4810 (2012).
22. Kovacevich, D. A. *et al.* Self-Limiting Electrospray Deposition for the Surface Modification of Additively Manufactured Parts. *ACS Appl Mater Interfaces* **12**, 20901–20911 (2020).
23. Lei, L. *et al.* Obtaining Thickness-Limited Electrospray Deposition for 3D Coating. *ACS Appl Mater Interfaces* **10**, 11175–11188 (2018).
24. Green-Warren, R. A. *et al.* Determining the Self-Limiting Electrospray Deposition Compositional Limits for Mechanically Tunable Polymer Composites. *ACS Appl Polym Mater* (2022).
25. Lee, J. H., Loya, P. E., Lou, J. & Thomas, E. L. Dynamic mechanical behavior of multilayer graphene via supersonic projectile penetration. *Science (1979)* **346**, 1092–1096 (2014).
26. Portela, C. M. *et al.* Supersonic impact resilience of nanoarchitected carbon. *Nat Mater* **20**, 1491–1497 (2021).
27. Canny, J. A Computational Approach to Edge Detection. *IEEE Trans Pattern Anal Mach Intell* **PAMI-8**, 679–698 (1986).
28. Lei, B. *et al.* Constructing Redox-Responsive Metal-Organic Framework Nanocarriers for Anticancer Drug Delivery. *ACS Appl Mater Interfaces* **10**, 16698–16706 (2018).
29. Gangineri Padmanaban, A. *et al.* Molecular-Weight-Dependent Interplay of Brittle-to-Ductile Transition in High-Strain-Rate Cold Spray Deposition of Glassy Polymers. *ACS Omega* **7**, 26465–26472 (2022).
30. Allcock, G., Dyer, P. E., Elliner, G. & Snelling, H. V. Experimental observations and analysis of CO2 laser-induced microcracking of glass. *J Appl Phys* **78**, 7295–7303 (1995).
31. Chan, E. P., Xie, W., Orski, S. V., Lee, J. H. & Soles, C. L. Entanglement Density-Dependent Energy Absorption of Polycarbonate Films via Supersonic Fracture. *ACS Macro Lett* **8**, 806–811 (2019).
32. Kim, A., Müftü, S., Thomas, E. L. & Lee, J.-H. Extreme Tribological Characteristics of Copolymers Induced by Dynamic Rheological Instability. *ACS Appl Polym Mater* (2021).
33. Veysset, D. *et al.* High-velocity micro-projectile impact testing. *Applied Physics Reviews* vol. 8 Preprint at https://doi.org/10.1063/5.0040772 (2021).
34. Papini, M. & Spelt, J. K. Organic coating removal by particle impact. *Wear* **213**, 185–199 (1997).
35. Yi, J., Boyce, M. C., Lee, G. F. & Balizer, E. Large deformation rate-dependent stress-strain behavior of polyurea and polyurethanes. *Polymer (Guildf)* **47**, 319–329 (2006).
36. Sun, Y., Kooi, S. E., Nelson, K. A., Hsieh, A. J. & Veysset, D. Impact-induced glass-to-rubber transition of polyurea under high-velocity temperature-controlled microparticle impact. *Appl Phys Lett* **117**, (2020).